

Optical far-infrared properties of graphene monolayer and multilayers

L.A. Falkovsky^{1,2} and C.C. Persheguba³

¹*L.D. Landau Institute for Theoretical Physics, Moscow 117334, Russia*

²*Institute of the High Pressure Physics, Troitsk 142190, Russia*

³*Moscow Institute of Physics and Technology, Dolgoprudniy 147100, Russia*

(Dated: February 11, 2013)

We analyze the features of the graphene mono- and multilayer reflectance in the far-infrared region as a function of frequency, temperature, and carrier density taking the intraband conductance and the interband electron absorption into account. The dispersion of plasmon mode of the multilayers is calculated using Maxwell's equations with the influence of retardation included. At low temperatures and high electron densities, the reflectance of multilayers as a function of frequency has the sharp downfall and the subsequent deep well due to the threshold of electron interband absorption.

PACS numbers: 81.05.Uw, 78.67.Ch, 78.67.-n

Monolayer and bilayer graphenes^{1,2,3} are gapless two-dimensional (2D) semiconductors^{4,5,6} whereas its 3D predecessor—graphite is a semimetal^{7,8,9}. Hence the dimensionality effects for the unique substance can be studied¹⁰. Monolayer graphene has a very simple electron band structure. Near the energy $\varepsilon = 0$, the energy bands are cones $\varepsilon_{1,2}(\mathbf{p}) = \pm vp$ at the K points in the 2D Brillouin zone with the constant velocity parameter $v = 10^8$ cm/s. Such a degeneration is conditioned by symmetry because the small group C_{3v} of the K points has two-dimensional representation.

While the carrier concentration is decreasing in the field gate experiment, the graphene conductivity at low temperatures goes to the finite minimal values^{1,2}. Much theoretical efforts^{11,12,13,14} have been devoted to evaluate the minimal conductivity in different approaches. Theoretical^{15,16,17} and experimental researches show that the main mechanism of the carrier relaxation is provided by the charged impurities and gives the collision rate $\tau^{-1} \sim 2\pi^2 e^4 n_{imp} / \hbar \epsilon_g^2 \varepsilon$, where ϵ_g is the dielectric constant of graphene, ε is the characteristic electron energy (of the order of the Fermi energy or temperature), and n_{imp} is the density of charged impurities per the unit surface. Plasmons in graphene are considered in Refs.^{18,19}. The optical visibility of both monolayer and bilayer graphene is studied in Ref.²⁰ focusing on the role of the underlying substrate.

In the present paper, we analyze the spectroscopy of the graphene monolayer and multilayers in the infra-red region. In order to calculate the reflection coefficient for the multilayers, we follow the method used in Ref.²¹ and determine the spectrum of electromagnetic excitations—plasmons. We use the appropriate boundary conditions at interfaces and the complex conductivity σ as a function of frequency ω , temperature T , and chemical potential μ . The chemical potential of ideal pure graphene equals to zero at any temperature. With the help of the gate voltage, one can control the density and type (n or p) of carriers varying their chemical potential.

The general expression for the conductivity used here is obtained in our previous paper¹⁸ and is valid under a restriction that the collision rate of carriers is less than

the frequency and spatial dispersion of the electric ac field, $\tau^{-1} \ll \omega, kv$. In limiting cases, our result coincides with the formulas of Ref.^{22,23}. For high frequencies, when one can also ignore the spacial dispersion of the ac field, $\omega \gg kv, \tau^{-1}$, the complex conductivity [see Eq. (8) in Ref.¹⁸] is given by

$$\sigma(\omega) = \frac{e^2 \omega}{i\pi \hbar} \left[\int_{-\infty}^{+\infty} d\varepsilon \frac{|\varepsilon|}{\omega^2} \frac{df_0(\varepsilon)}{d\varepsilon} - \int_0^{+\infty} d\varepsilon \frac{f_0(-\varepsilon) - f_0(\varepsilon)}{(\omega + i\delta)^2 - 4\varepsilon^2} \right]. \quad (1)$$

Here, the first term corresponds to the intraband electron–photon scattering processes. One can obtain it from the Drude–Boltzmann expression (for a case $1/\tau = 0$) and write explicitly:

$$\sigma^{intra}(\omega) = i \frac{2e^2 T}{\pi \hbar \omega} \ln [2 \cosh(\mu/T)]. \quad (2)$$

The second term in Eq. (1), where $\delta \rightarrow 0$ is the infinitesimal quantity determining the bypass around the integrand pole, owes its origin to the direct interband electron transitions. The real part of this contribution is reduced to the expression for the absorbed energy due to the interband transitions. Since there is no gap between the conduction band and valence band, these two terms can compete and the interband contribution becomes larger at high frequencies $\omega > T, \mu$. In the opposite case, the intraband contribution plays the leading role.

The difference of the Fermi functions in the second integrand equals to

$$G(\varepsilon) = \frac{\sinh(\varepsilon/T)}{\cosh(\mu/T) + \cosh(\varepsilon/T)}.$$

Extracting the principal value of the integral, we arrive at the integral without singularities and write the interband conductivity in the form available for numerical calculations:

$$\sigma^{inter}(\omega) = \frac{e^2}{4\hbar} \left[G(\omega/2) - \frac{4\omega}{i\pi} \int_0^{+\infty} d\varepsilon \frac{G(\varepsilon) - G(\omega/2)}{\omega^2 - 4\varepsilon^2} \right]. \quad (3)$$

Here, the first term is given asymptotically by

$$G(\omega/2) = \begin{cases} \tanh(\omega/4T), & \mu \ll T, \\ \theta(\omega - 2\mu), & \mu \gg T, \end{cases} \quad (4)$$

where the step-function $\theta(\omega - 2\mu)$ expresses the condition for the interband electron transitions at low temperatures. The integral in Eq. (3) represents the imaginary interband correction to the intraband conductivity.

By using the gate voltage, one can control the density of electrons (n_0) or holes ($-n_0$). Then the chemical potential is determined by the condition

$$n_0 = \frac{2}{\pi(\hbar v)^2} \int_0^{+\infty} \varepsilon [f_0(\varepsilon - \mu) - f_0(\varepsilon + \mu)] d\varepsilon. \quad (5)$$

From this expression and Fig. 1(a), one can see that the chemical potential goes to zero while the temperature increases.

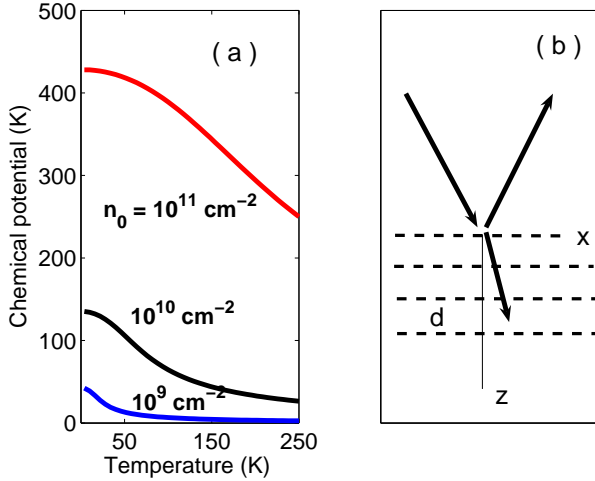


FIG. 1: (a) Chemical potential (in K) as a function of temperature at carrier densities noted at curves. (b) Multilayers sample and geometry of wave scattering.

In order to calculate the graphene reflectance, we apply Maxwell's equations

$$\nabla(\nabla \cdot \mathbf{E}) - \nabla^2 \mathbf{E} = \epsilon_0 \frac{\omega^2}{c^2} \mathbf{E} + \frac{4\pi i \omega}{c^2} \mathbf{j}, \quad (6)$$

where ϵ_0 is the ion contribution into the dielectric constant and \mathbf{j} is the conductivity current. We consider the case of the p -polarization, when the field \mathbf{E} lies in the xz plane and the current \mathbf{j} has only the in-layer x component (see Fig 1b).

(i) *Optics of a monolayer.* Consider the graphene monolayer at $z = 0$ with $\epsilon_0 = \epsilon_g$ deposited on the substrate ($z > 0$) with the dielectric constant $\epsilon_0 = \epsilon_s$. In the vacuum, $z < 0$, the ac field is given by the sum of incident and reflected waves and by the transmitted wave

in the substrate. In the geometry considered, the current in graphene monolayer can be written in the form

$$j_x = \sigma \delta(z) E_x. \quad (7)$$

Making use of the Fourier transformations with respect to the x coordinate, $\mathbf{E} \propto e^{ik_x x}$, we rewrite the Maxwell equations (6) as follows

$$\begin{aligned} ik_x \frac{dE_z}{dz} - \frac{d^2 E_x}{dz^2} - \epsilon_0 \frac{\omega^2}{c^2} E_x &= \frac{4\pi i \omega}{c^2} j_x, \\ ik_x \frac{dE_x}{dz} + (k_x^2 - \epsilon_0 \frac{\omega^2}{c^2}) E_z &= 0. \end{aligned} \quad (8)$$

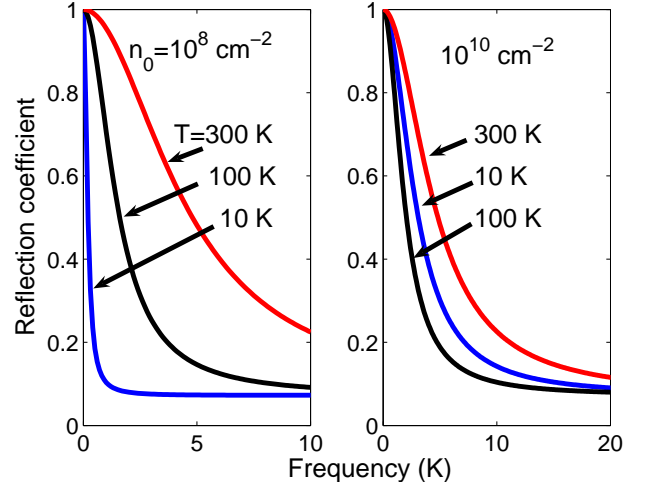


FIG. 2: Reflectance from the graphene monolayer with carrier densities $n_0 = 10^8 \text{ cm}^{-2}$ (left) and $n_0 = 10^{10} \text{ cm}^{-2}$ (right) versus the frequency at temperatures noted at the curves; normal incidence.

The boundary conditions for these equations at $z = 0$ are the continuity of the field component E_x and the jump of the electric-induction z component ϵE_z at sides of the monolayer:

$$\epsilon_s E_z|_{z=+0} - E_z|_{z=-0} = 4\pi \int_{-0}^{+0} \rho(\omega, k_x, z) dz. \quad (9)$$

The carrier density is connected to the current in Eq. (7) according to the continuity equation

$$\rho(\omega, k_x, z) = j_x(\omega, k_x, z) k_x / \omega.$$

Substituting E_z from the second Eq. (8) into (9), we find the second boundary condition

$$\frac{\epsilon_s}{k_s^2} \frac{dE_x}{dz} \Big|_{z=+0} - \frac{1}{(k_z^i)^2} \frac{dE_x}{dz} \Big|_{z=-0} = \frac{4\pi\sigma(\omega)}{i\omega} E_x \Big|_{z=0}, \quad (10)$$

where

$$k_s = \sqrt{\epsilon_s(\omega/c)^2 - k_x^2}, \quad k_z^i = \sqrt{(\omega/c)^2 - k_x^2}.$$

Using the boundary conditions, we find the reflection amplitude

$$r = \frac{1 - C}{1 + C}, \quad (11)$$

where $C = k_z^i [4\pi\sigma(\omega)/\omega + (\epsilon_s/k_s)]$.

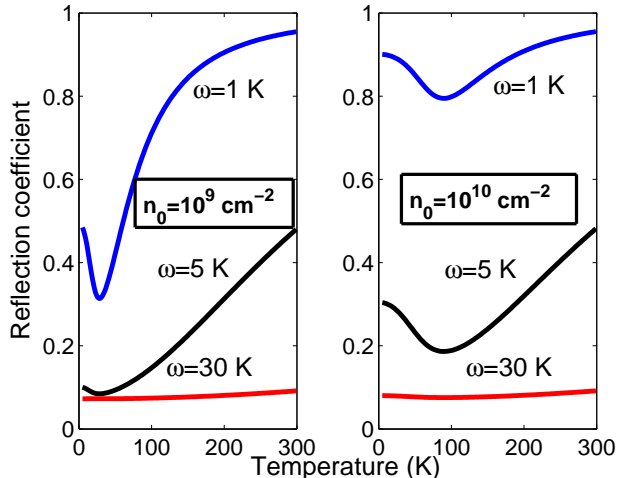


FIG. 3: Reflectance from the graphene monolayer with carrier concentrations $n_0 = 10^9 \text{ cm}^{-2}$ (left) and 10^{10} cm^{-2} (right) versus temperature for frequencies noted at curves; normal incidence.

The reflection coefficient calculated with the help of Eqs. (1)–(5) and (11) for normal incidence is shown in Figs. 2 and 3 as a function of frequency, temperature, and carrier concentration. Notice the different temperature behavior of reflectance from the samples containing the low and high carrier densities. Reflectance for the lower carrier density (Fig. 2, left) is larger at higher temperatures. This corresponds to the increase in the intraband conductivity (giving the main contribution here) with temperature [see Eq. (2) for $\mu \ll T$]. At the larger carrier concentration (Fig. 2, right), the chemical potential (decreasing with temperature, see Fig. 1a) plays the important role appearing in Eq. (2) instead of T . Therefore, the curve for lowest temperature $T = 10 \text{ K}$ is between the curves for $T = 100 \text{ K}$ and 300 K in this case. The temperature dependencies of reflectance are not monotonic as clearly seen in Fig. 3.

The optical properties of the graphene bilayer can be considered in a similar way. Here we do not present the corresponding results and investigate another 3D example—the graphene multilayers.

(ii) *Spectroscopy of graphene multilayers.* Let the multilayers cross the z axis at points $z_n = nd$, where d is the distance between the layers (see Fig. 1b). Such a system can be considered as a model of graphite since the distance $d = 3\text{\AA}$ in graphite is larger than the interatomic distance in the layer. So we describe the carrier interaction in the presence of ac electric field with the help of

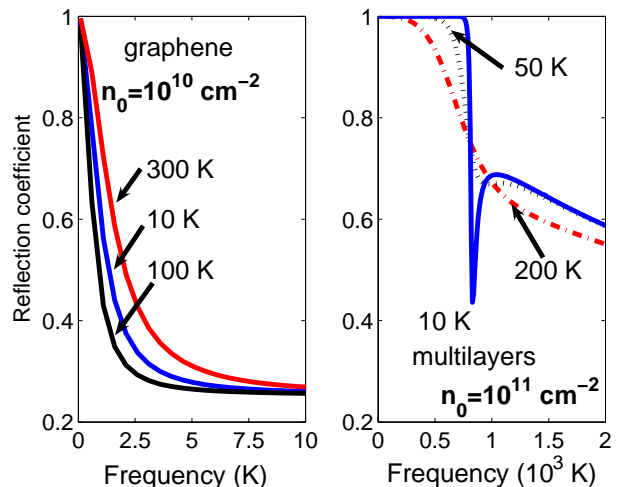


FIG. 4: Reflectance from the graphene monolayer with the carrier density $n_0 = 10^{10} \text{ cm}^{-2}$ (left) and multilayers with $n_0 = 10^{11} \text{ cm}^{-2}$ in a layer and distance $d = 3\text{\AA}$ between layers (right); temperatures are noted at curves, the incidence angle is 80° .

self-consistent Maxwell's equations (6). For the x component of the field E_x , they give

$$\left(\frac{d^2}{dz^2} + k_s^2 + 2k_s \mathcal{D} \sum_n \delta(z - nd) \right) E_x = 0, \quad (12)$$

where $\mathcal{D} = 2i\pi\sigma(\omega)k_s/\epsilon_g\omega$.

For the infinite number of layers in the stack, the solutions of Eq. (12) represent two Bloch states

$$e_{1,2}(z) = e^{\pm ik_z nd} \{ \sin k_s(z - nd) - e^{\mp ik_z d} \times \sin k_s[z - (n+1)d] \}, \quad nd < z < (n+1)d \quad (13)$$

with the quasi-momentum k_z determined from the dispersion equation

$$\cos k_z d = \cos k_s d - \mathcal{D} \sin k_s d. \quad (14)$$

The dispersion equation describes the electric field excitations of the system, i.e., plasmons. The quasi-momentum k_z can be restricted to the Brillouin half-zone $0 < k_z < \pi/d$, if the parameter \mathcal{D} is real. In the general case, while taking the interband absorption into account, we fix the choice of the eigen-functions in Eq. (13) by the condition $\text{Im} k_z > 0$ so that the solution e_1 decreases in the positive direction z .

Reflectance from the multilayers occupied the semi-space $z > 0$ can be calculated similarly to the reflectance of a monolayer. The electric field is given by the decreasing solution e_1 inside the sample and by the sum of incident and reflected waves in the vacuum, $z < 0$, with the same value of the component k_x .

Using the boundary condition, Eq. (10), with the dielectric constant of graphene ϵ_g instead of ϵ_s , we find the

reflected amplitude

$$r = \frac{i \sin(k_s d) - Z}{i \sin(k_s d) + Z},$$

where

$$Z = \epsilon_g \frac{k_z^i}{k_s} [\cos(k_s d) - e^{-ik_z d}],$$

k_z^i is the normal component of wavevector in the vacuum and k_z is the quasi-momentum determined by the dispersion equation(14) at fixed values of ω and k_x .

In Fig. 4, the reflection coefficient calculated for multilayers is shown in comparison with the reflection coefficient of the monolayer. The left panel in this figure differs from the right one in Fig. 2 only in the incidence angle which is now taken to be 80° in order to emphasize the multilayer features. The main of them is the sharp downfall of reflectance at low temperatures (see the right

panel in Fig. 4). This is the threshold effect of the direct interband transitions at $\omega \geq 2\mu$, which is sharp when temperature $T \rightarrow 0$ [see Eq. (4)]. Just after the downfall, the reflectance has the deep well which disappears while the temperature increases. Then the downfall becomes more smooth. Notice that observations of the absorption threshold provide a direct method of carrier density characterization of graphene $n_0 = (\mu/\hbar v)^2/\pi$.

In conclusion, we have developed the detailed microscopic theory of the graphene mono- and multilayer spectroscopy. We have shown that the nonmonotonic temperature behavior of reflectance from the monolayer in the infra-red region is expected. We have argued that at low temperatures and high electron densities, the reflectance from multilayers has the sharp downfall with the subsequent deep well. They are caused by the direct interband electron transitions.

This work is supported by the Russian Foundation for Basic Research (grant No.07-02-00571).

-
- ¹ K.S. Novoselov, A.K. Geim, S.V. Morozov, D. Jiang, M.J. Katsnelson, I.V. Grigorieva, S.V. Dubonos, and A.A. Firsov, *Science* **306**, 666 (2004); *Nature (London)* **438**, 197 (2005).
- ² Y. Zhang, J.P. Small, M.E.S. Amory, P.Kim, *Phys. Rev. Lett.* **94**, 176803 (2005); *Nature (London)* **438**, 201 (2005).
- ³ K.S. Novoselov, E. McCann, S.V. Morozov, V.I. Fal'ko, M.J. Katsnelson, U. Zeitler, D. Jiang, F. Shedin, and A.K. Geim, *Nat. Phys.* **2**, 177 (2006).
- ⁴ M.S. Dresselhaus and G. Dresselhaus, *Adv. Phys.* **51**, 1 (2002).
- ⁵ N. Ando, *J. Phys. Soc. Jpn.* **74**, 777 (2005).
- ⁶ E. McCann and V.I. Fal'ko, *Phys. Rev. Lett.* **96**, 086805 (2006).
- ⁷ P.R. Wallace, *Phys. Rev.* **71**, 622 (1947).
- ⁸ J.C. Slonczewski and P.R. Weiss, *Phys. Rev.* **99**, 636(A) (1955).
- ⁹ J.W. MacClure, *Phys. Rev.* **104**, 666 (1956).
- ¹⁰ E. Fradkin, *Phys. Rev. B* **33**, 3263 (1986).
- ¹¹ P.A. Lee, *Phys. Rev. Lett.* **71**, 1887 (1993).
- ¹² A.W.W. Ludwig, M.P.A. Fisher, R. Shankar, G. Grinstein, *Phys. Rev. B* **50**, 7526 (1994).
- ¹³ J. Tworzydło et al., *Phys. Rev. Lett.* **96**, 246802 (2006).
- ¹⁴ K. Ziegler, cond-mat/0604537.
- ¹⁵ N. Ando, *J. Phys. Soc. Jpn.* **75**, 074716 (2006).
- ¹⁶ K. Nomura, A.H. MacDonald, cond-mat/0606589.
- ¹⁷ N.M.R. Peres, F. Guinea, A.Y. Castro Neto, *Phys. Rev. B* **73**, 125411 (2006); J. Nilsson, A.Y. Castro Neto, F. Guinea, and N.M.R. Peres, *Phys. Rev. Lett.* **97**, 266801 (2006).
- ¹⁸ L.A. Falkovsky and A.A. Varlamov, cond-mat/0606800, *Eur. Phys. J. B* **56**, 281 (2007).
- ¹⁹ E.H. Hwang and S. Das Sarma, *Phys. Rev. B* **75**, 205418 (2007).
- ²⁰ D.S.L. Abergel, A. Russell, and V. I. Fal'ko, cond-mat/0705.0091, unpublished.
- ²¹ L.A. Falkovsky and E.G. Mishchenko, *JETP Letters* **82**, 96 (2005).
- ²² V.P. Gusynin, S.G. Sharapov, and J.P. Carbotte, *Phys. Rev. B* **75**, 165407 (2007); cond-mat/0607727, *Phys. Rev. Lett.* **96**, 256802 (2006).
- ²³ J. Cserti, *Phys. Rev. B* **75**, 033405 (2007).